Title

Measurement of coherent vibrational dynamics with X-ray Transient Absorption Spectroscopy simultaneously at the Carbon K- and Chlorine L2,3- edges

Journal
Communications Physics, 7(1)

ISSN
2399-3650

Authors
Ross, Andrew D
Hait, Diptarka
Scutelnic, Valeriu
et al.

Publication Date
2024

DOI
10.1038/s42005-024-01794-4

Peer reviewed

communications physics

Article

https://doi.org/10.1038/s42005-024-01794-4

Measurement of coherent vibrational dynamics with X-ray Transient Absorption Spectroscopy simultaneously at the Carbon K- and Chlorine $L_{2,3}$- edges

Andrew D. Ross[1,2,4,6], Diptarka Hait[1,2,5,6], Valeriu Scutelnic[1,2], Daniel M. Neumark[1,2], Martin Head-Gordon[1,2] & Stephen R. Leone[1,2,3] ✉

X-ray Transient Absorption Spectroscopy (XTAS) is a powerful probe for ultrafast molecular dynamics. The evolution of XTAS signal is controlled by the shapes of potential energy surfaces of the associated core-excited states, which are difficult to directly measure. Here, we study the vibrational dynamics of Raman activated CCl_4 with XTAS targeting the C 1s and Cl 2p electrons. The totally symmetric stretching mode leads to concerted elongation or contraction in bond lengths, which in turn induce an experimentally measurable red or blue shift in the X-ray absorption energies associated with inner-shell electron excitations to the valence antibonding levels. The ratios between slopes of different core-excited potential energy surfaces (CEPESs) thereby extracted agree very well with Restricted Open-Shell Kohn-Sham calculations. The other, asymmetric, modes do not measurably contribute to the XTAS signal. The results highlight the ability of XTAS to reveal coherent nuclear dynamics involving < 0.01 Å atomic displacements and also provide direct measurement of forces on CEPESs.

X-ray absorption spectroscopy is a powerful instrumental technique[1–4] that has been used to measure atomic structure, electronic dynamics, and nuclear motion[1,5–18]. The interpretation of experimental X-ray absorption is often done through comparison to quantum chemical calculations, leading to considerable recent theoretical interest in this area[19–33]. However, most computational work has focused on predicting X-ray absorption energies at fixed, often equilibrium, geometries, and changes in core-level excitation energies with nuclear displacements have been relatively unexplored, in large part due to the relative lack of high-quality experimental data for straightforward comparison. Unambiguously attributing vibronic effects in spectral lineshapes[34–38] to individual normal modes is challenging for polyatomic systems. Spectra collected from X-ray probing of photoinduced dynamics[6,7,14,33,39] and X-ray emission processes[40,41] often show signatures of significant nuclear dynamics, but modeling such nonequilibrium phenomena poses a challenge independent of the X-ray spectrum prediction problem. It would therefore be useful to have experimental measurements that unambiguously report variations in core-excitation energies vs specific nuclear displacements and thereby provide information about core-excited potential energy surfaces (CEPESs).

A relatively straightforward route to obtaining CEPES properties is through X-ray Transient Absorption Spectroscopy (XTAS) of coherent vibrational dynamics. Such dynamics can be experimentally realized by first exciting the sample to a superposition of vibrational states by Impulsive Stimulated Raman Scattering (ISRS), where a pump pulse, such as the short 800 nm pulse shown in Fig. 1, launches a wavepacket along the Raman active vibrational modes that have a period more than double the duration of the pump laser pulse[42,43]. Following the pump pulse, the nuclear wavepackets oscillate with the associated normal mode frequencies as coherent states of the harmonic oscillator, assuming the harmonic approximation holds and the modes do not couple. As the molecule vibrates, changes in the core-level excitation energies can be tracked by the soft X-ray probe at a series of delay times from the initial excitation, revealing features of the CEPES.

The connection between transient core-level excitation energy changes and CEPES features can be understood within a simple Born-Oppenheimer

---

[1]Department of Chemistry, University of California Berkeley, Berkeley, CA, 94720, USA. [2]Chemical Sciences Division, Lawrence Berkeley National Laboratory, Berkeley, CA, 94720, USA. [3]Department of Physics, University of California Berkeley, Berkeley, CA, 94720, USA. [4]Present address: Toptica Photonics, Inc., Pittsford, NY, 14534, USA. [5]Present address: Department of Chemistry and PULSE Institute, Stanford University, Stanford, CA, 94305, USA. [6]These authors contributed equally: Andrew D. Ross, Diptarka Hait. ✉e-mail: srl@berkeley.edu

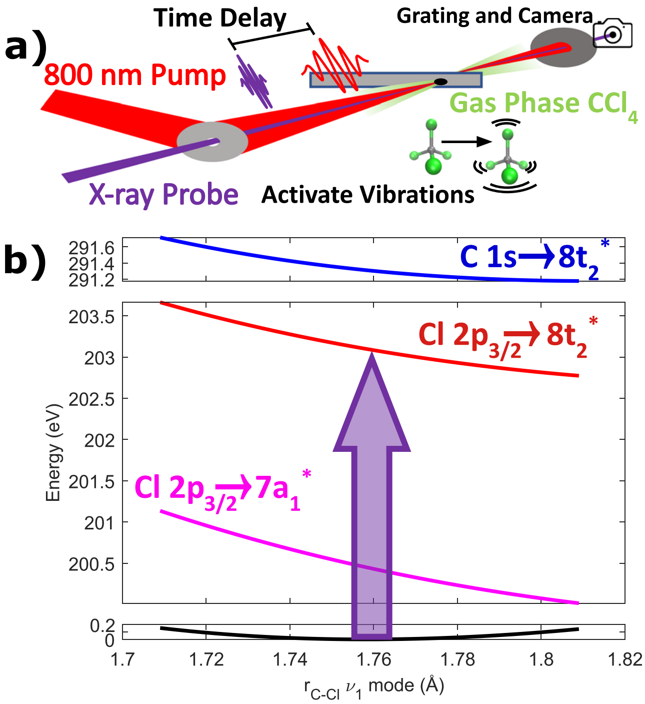

Fig. 1 | Outline of the experiment. a Diagram of the experiment. Gas phase CCl_4 is vibrationally excited with a 6 fs duration 800 nm pump and is probed after a variable delay with a few-fs X-ray probe pulse, which is dispersed via a grating onto a CCD camera. **b** Schematic of the transitions studied along the CCl_4 symmetric stretch (ν_1) mode, with associated PES (y axis energy spacings to scale). The experimentally measured excitation energy is $\Omega_C(q) = E_C(q) - E_G(q)$. Note that the $E_G(q)$ surface has zero slope at the equilibrium bond length.

model of classical nuclei moving on electronic potential energy surfaces. Let the molecule be distorted by $\{q_i\}$ along each of the ground state normal modes $\{i\}$ relative to the equilibrium geometry in the electronic ground state. The corresponding core-excitation energy is therefore $\Omega_C(\{q_i\}) = E_C(\{q_i\}) - E_G(\{q_i\})$, where E_C and E_G are potential energy surface functions for the core-excited and ground electronic states, respectively. $E_G(\{q_i\})$ does not have any terms linear in $\{q_i\}$ as the undistorted geometry is a minimum on the electronic ground state potential energy surface. This is not true for $E_C(\{q_i\})$, as minima on the CEPES (if they exist at all) are unlikely to be identical with the electronic ground state equilibrium geometry[44–48]. For small displacements therefore:

$$E_C(\{q_i\}) \approx E_C(0) + \sum_i q_i \left(\frac{\partial E_C}{\partial q_i}\right)_{\{q_i\}=0} \tag{1}$$

where $\left(\frac{\partial E_C}{\partial q_i}\right)_{\{q_i\}=0}$ is the slope of the CEPES at the ground state equilibrium geometry along the i^{th} ground state mode, and higher order terms in $\{q_i\}$ are neglected. The excitation energies are similarly:

$$\Omega_C(\{q_i\}) \approx E_C(0) - E_G(0) + \sum_i q_i \left(\frac{\partial E_C}{\partial q_i}\right)_{\{q_i\}=0} \tag{2}$$

For coherent vibrational motions within the harmonic approximation, the pump stimulated displacements evolve in time as $q_i(t) = A_i \cos(\omega_i t + \phi_i)$. A Fourier transform of the time-dependent excitation energies $\Omega_C(\{q_i(t)\})$ would therefore reveal information about the CEPES slopes. Specifically, let us consider two core-excited states C_1 and C_2, with associated time-dependent core-excitation energies $\Omega_{C_1}(t)$ and $\Omega_{C_2}(t)$ resulting from vibrational dynamics. For a given ground state normal mode i with ground state frequency ω_i, the ratio of the associated Fourier transforms $\mathcal{F}$ then are:

$$\frac{\mathcal{F}\left[\Omega_{C_1}(t)\right](\omega_i)}{\mathcal{F}\left[\Omega_{C_2}(t)\right](\omega_i)} = \frac{\left(\frac{\partial E_{C_1}}{\partial q_i}\right)_{\{q_i\}=0}}{\left(\frac{\partial E_{C_2}}{\partial q_i}\right)_{\{q_i\}=0}} \tag{3}$$

indicating that the ratio of the Fourier transforms of two time-dependent core-excitation energies arising from vibrational dynamics is equivalent to the ratio of the CEPES slopes along that mode at the ground state equilibrium geometry. We note that anharmonic effects may lead to deviations from this simplified model, but we do not consider this aspect further in this work.

XTAS has been used to observe coherent vibrational motion in the past[2,49–52] and specifically the CEPES for SF_6 at the S $L_{2,3}$ edges recently[53,54]. In this work, we experimentally measure the relative CEPES slopes along the symmetric stretching mode of CCl_4, considering both the C K-edge (1s, ~ 285 eV) and the Cl $L_{2,3}$-edge (2p, ~ 200 eV). We focus on dipole allowed core-excitations to the antibonding $7a_1^*$ and (triply degenerate) $8t_2^*$ levels, which are energetically well separated from each other and readily accessible with the X-ray probe[55,56] (as shown in Fig. 1b). Relative CEPES slopes from experiment are compared to the corresponding ratios obtained from absolute CEPES slopes predicted by restricted open-shell Kohn-Sham (ROKS[19,57]) calculations. The computed values are found to lie within the experimental error bars, indicating an excellent level of agreement and permitting estimation of absolute experimental CEPES slopes. No signal in the experimental X-ray absorption energy is detected for the other normal modes, as no net displacement along these modes is induced by the pump pulse.

Methods

Experiment

The experimental apparatus has been fully described in ref. 58. Here, we provide a brief summary of the relevant experimental conditions. The X-ray probe is a nearly femtosecond pulse with photon energies extending up to 370 eV, generated by high harmonic generation (HHG) by a 10 fs, 1300 nm pulse. ISRS is induced by an 800 nm pulse, spectrally broadened, and compressed to about 6 fs in duration with a 1 kHz repetition rate. The maximum power used on the sample was 150 mW, focused to 65 μm full width at half maximum (FWHM), which gives an electric field with peak intensity up to $3 \pm 1 \times 10^{14}$ W cm^{-2} as estimated by numerical calculations (details are given in Supplementary Notes 4) and by observed relative ionization rates of Ar. We note that this intensity corresponds to a peak electric field strength of 3.4 ± 1.1 V Å^{-1} (i.e, 0.065 ± 0.022 a.u.). The X-ray monochromator has 0.2 eV spectral resolution at the C K-edge and 0.1 eV resolution at the Cl $L_{2,3}$-edge. The experimental data are measured as a change in absorbance, or ΔOD. The temporal cross-correlation of the experiment is measured to be 8 ± 2 fs by the autoionization in Ar $L_{2,3}$ lines[59]. Experiments are performed over different time ranges to cover a wider range of dynamics; the shortest have a step size of 1 fs and extend to 80 fs and the longest have variable step sizes and extend to 10 ps. Additionally, experiments are run with varying pump power, from ~ $1-3 \times 10^{14}$ W cm^{-2}, to assess how the power affects the temporal dynamics. Each scan that has a different combination of pump powers, time step sizes, and gas pressures is referred to as a "data set" in this paper. These data sets are taken as closely in time as possible to make the comparisons between them more consistent. CCl_4 was obtained from Sigma-Aldrich at 99.5% purity. We note that some of the CCl_4 is strong-field ionized under experimental conditions, leading to dissociative dynamics that have been detailed in ref. 7.

The experimental data are noise filtered by two separate noise reduction algorithms, which are fully defined in Supplementary Notes 1. In brief, the first is "edge referencing," which involves using a region with no absorption signal and referencing it to find the correlated noise of the experiment. Then, the correlated noise is subtracted from the data[60]. The second noise reduction is Fourier filtering, wherein a low-pass Fourier filtered spectrum is used as the reference spectrum when calculating ΔOD, instead of a true pump-off reference[61]. This method reduces noise associated with fluctuations in X-ray flux from pulse to pulse and allows for better comparison of subsequent time points, critical for observation of vibration signals. Neither of these noise reduction algorithms correlates data between different time points; they only improve the ΔOD signal within a single time point, so no spurious Fourier transform signals should be introduced by these techniques.

The method for obtaining the CEPES slopes from the measured data involves the use of a purpose-built processing software. It starts by separating out the static OD data into a sum of Gaussians, as shown in Fig. 2. The ΔOD data are simulated by moving the Gaussians in time according to a sine wave, corresponding to the vibration frequency with amplitude as a variable for the slopes in question. The difference between the simulated spectra OD and the measured static ground state OD reproduces the entire ΔOD, across multiple data sets simultaneously. The algorithm is able to concurrently simulate the ΔOD data for dissociation of CCl_4^+ and both the edge referencing and Fourier filtering noise reduction techniques, so any errors that might arise from either are minimized. Each fit includes convolution with a Gaussian of 8 fs FWHM to account for the temporal cross-correlation of the experiment and uses 95% confidence intervals as error bars. A full explanation of the fitting algorithm is provided in Supplementary Notes 1.

Computational

Quantum chemical calculations were performed with the Q-Chem software package[62], using the SCAN0 functional[63] as it is accurate for the computation of both core-excitation energies[19,64] and polarizabilities[65]. The equilibrium geometry and harmonic normal modes were found with the aug-pcseg-2 basis set[66]. We note that the four lowest energy unoccupied canonical molecular orbitals at this level of theory are antibonding in character and correspond to the $7a_1^*$ and $8t_2^*$ levels. ROKS calculations for core-excited states were carried out with the same functional, and a mixed basis approach[19] of using the decontracted aug-pcX-2 basis[67] on the atom type involved in the core-excitation and aug-pcseg-2 on the other atom (i.e. Cl L-edge calculations utilized aug-pcX-2 on Cl and aug-pcseg-2 on C). Scalar relativistic effects in the core-excitation energy were accounted for with the exact two-component (X2C) method[68,69]. Spin-orbit effects in the Cl L-edge were simulated in the manner described in ref. 19. Excited state orbital optimization was done with the square gradient minimization (SGM) algorithm[70]. Local exchange-correlation integrals were calculated over a radial grid with 99 points and an angular Lebedev grid with 590 points. The CEPES slopes vs symmetric bond stretch were explicitly obtained by fitting the computed core-level excitation energies against the C-Cl bond length for a set of geometries spanning ± 0.01 Å change from the computed equilibrium separation of 1.759 Å, in increments of 0.001 Å. Fitting over a larger range of bond lengths (± 0.05 Å vs equilibrium) yielded very similar slopes (as shown in Supplementary Data 1).

Results and Discussion

Normal modes of CCl_4

The experimental and computed normal modes of CCl_4 are reported in Table 1, and they are in reasonable agreement. All of the normal modes are Raman active[71–73] and have periods ranging from 42 fs (asym. stretch, ν_3) to 153 fs (e bend, ν_2). This indicates that they should all be stimulated by the 6 fs duration 800 nm pump pulse.

General features of experimental spectra

The ground state static X-ray absorption of CCl_4 is shown in Fig. 2. It shows the experimentally measured spectra and the separation of electronic transitions as sums of Voigt functions[74,75] for both the Cl $L_{2,3}$-edge ($2p_{3/2}^{-1}$ and $2p_{1/2}^{-1}$ starting at 200 eV) and the C K-edge ($1s^{-1}$ starting around 285 eV[55]). The Voigt functions are determined by fit, and at the Cl $L_{2,3}$-edge we use a second shifted profile with a different amplitude to model the spin-orbit (s-o) splitting of 1.6 eV. The spin-orbit area ratio differs from the expected 2:1 for the L_3:L_2[76], which is not unusual for some of these edges[77]. The spectral peak assignments are given in Table 2[78,79].

The main features of interest in the Cl L-edge are Peaks 1 and 2 at 200.35 and 203.15 eV, which correspond to excitations to the $7a_1^*$ and $8t_2^*$ orbitals, respectively. Peak C_1 is the only feature of interest in the C K-edge, and it arises from the C 1s→ $8t_2^*$ excitation. Unfortunately, the C 1s→ $7a_1^*$ excitation is not a dipole allowed transition and so it cannot be probed by our experiment[55]. In the Cl absorption, there are additional peaks, Peaks 3 and 4, that arise due to Rydberg transitions and shape resonances[55]; although, the corresponding transient spectral features do not show prominent vibrational oscillations comparable to Peaks 1 and 2. The Cl L_1-edge

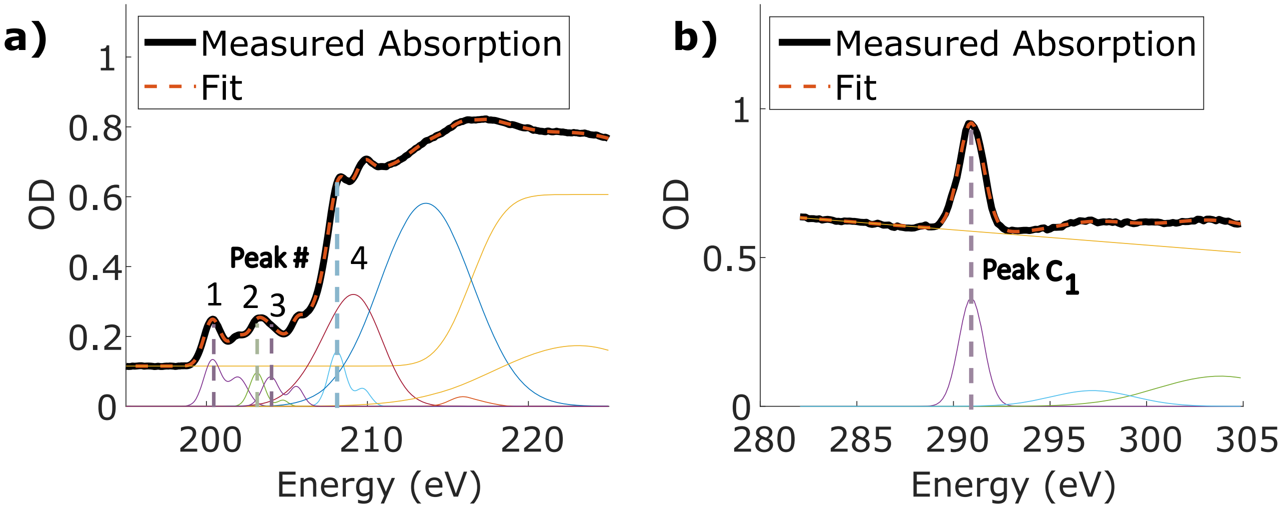

Fig. 2 | Static X-ray absorption of CCl_4. **a** Cl $L_{2,3}$-edges and **b**) C K-edge (OD stands for optical density). Additionally, a breakdown of the net absorption into the individual transitions (represented by colored Gaussians) is shown (assignments provided in Table 2). Cl L_3 and L_2 excitation peaks have a spin-orbit induced separation of 1.6 eV. Extra Gaussians after the rising edge were used to better reproduce the measured data. The fit (red dashed line) agrees very well with the experimental measurement (black solid line).

Table 1 | Comparison of experimental[72] and computed (this work) normal mode frequencies for CCl_4

Symmetry	Character	Experimental ω (in cm^{-1})	Computed ω (in cm^{-1})
e	bend	218.0 (ν_2)	224.0 225.0
t_2	bend	309.7 (ν_4)	325.6 325.7 326.0
a_1	sym. stretch	456.6 (ν_1)	477.9
t_2	asym. stretch	790.6 (ν_3)	791.9 794.2 798.6

The values are generally in good agreement. The degeneracy of normal modes is broken by the use of a finite grid for computation of DFT exchange-correlation integrals, which breaks rotational invariance. As a result, nine distinct frequencies are obtained from computation, clustered into four groups (ν_{1-4}) corresponding to the experimental frequencies.

Table 2 | Assignment of peaks in static X-ray absorption

Peak Assignments			
Peak	**Exp. Energy (eV)**	**Calc. Energy (eV)**	**Assignment**
1	200.35	200.44	Cl $2p_{3/2} \rightarrow 7a_1^*$
1_{s-o}	201.95	202.05	Cl $2p_{1/2} \rightarrow 7a_1^*$
2	203.15	203.09	Cl $2p_{3/2} \rightarrow 8t_2^*$
2_{s-o}	204.75	204.70	Cl $2p_{1/2} \rightarrow 8t_2^*$
3	203.98	-	Cl Rydberg
3_{s-o}	205.58	-	Cl Rydberg
4	208.1	-	Shake-up State
4_{s-o}	209.7	-	Shake-up State
C_1	290.91	291.30	C 1s$\rightarrow 8t_2^*$

The assignments of the fitted absorption components from ROKS calculations (peaks 1, 2 and C_1) and previous literature[78,79] (for other peaks that are not considered further in this work). The Cl L_2-edge (s-o peaks) are 1.6 eV higher in energy than the corresponding the L_3-edge peaks due to spin-orbit effects.

(~260 eV) involving the 2s orbitals is also accessible with the probe, but that edge is too broad to extract useful information, especially for vibrational dynamics, where the transient signal strength resulting from coherent vibrational motion is proportional to the sharpness of the static absorption. In the static absorption, a downside of measuring simultaneous element absorptions becomes apparent; the absorption from the ionization of Cl inner-shell electrons extends all the way to the C K-edge, where it represents ~50% of the absorption, even at the point of highest carbon absorption. This leads to smaller effective photon flux available at the C K-edge and increases the relative noise.

The time-resolved changes to the static absorption spectrum, or ΔOD, after excitation with the few-fs 800 nm pump pulse are shown in Fig. 3. The blue areas show where the absorption decreases, and the red are where absorption increases. Several transient spectral features that are relatively constant in time after $t = 0$ are apparent in both the Cl and C edges. These features arise from CCl_4^+ formed by pump induced strong-field ionization, whose Jahn-Teller and dissociative dynamics have already been studied in detail in a previous work[7].

The ΔOD signals that are of interest to this paper are the oscillatory signals that occur surrounding the electronic transition peaks and their spin-orbit splittings at 200.35 eV, 203.15 eV, and 290.91 eV from Peaks 1, 2, and C_1, respectively. The positive-negative-etc. oscillations in time that are typical of vibrational features in XTAS[53] are clear at 200.35 eV in Fig. 3 a) but are not as clear at some of the other energies, especially at the C K-edge. This is because of obscuring transient absorption from ionized species. We were not able to obtain high quality pure vibrational signals without also inducing substantial strong-field ionization. The effect of the cation signals are however accounted for in the fitting program, and the existence of the oscillations can be confirmed by the lower panels in Fig. 3, which show the Fourier transform in time at the different probe energies. Signals above the noise are apparent at 456 cm^{-1} (73.05 fs), corresponding to the totally symmetric a_1 symmetry mode[72], with the pink dotted oval aiding the eye. The Fourier transform signals appear as doublets to either side of the static absorption peak, but not at the peak center, as is most clear at 200.35 eV. This is due to the nature of these signals, which occur by essentially shifting the absorption peak center energy to higher and lower energies as the molecule vibrates. The edges of the absorption peak, where the derivative of absorption vs energy is the largest, produce the greatest signal, while the middle of the absorption peaks produce the smallest signal, as the derivative goes to zero.

At longer times than those shown in Fig. 3, ~3 ps, the different isotopic masses of Cl lead to dephasing and an inability to distinguish vibrations. At 10.5 ps, the various frequencies of different isotopes rephase as expected[73,80] and the signal can be seen again, as shown in Supplementary Notes 1.3 and Supplementary Fig. S5. However, most data taken focus on the < 1 ps range to circumvent this dephasing effect.

Notably, the Fourier transform does not reveal signals at frequencies corresponding to the e and t_2 symmetry vibrations, for reasons that are discussed later. Fourier transformation of XTAS data often amplifies noise, so some regions may appear to show additional signals; however, extensive repetition of the experiment only shows reproducibility in the signals reported, and some additional data sets are shown in Supplementary Figs. S2, S4, and S5.

Core-excited potential slopes vs symmetric stretch

The experimentally measured signals were analyzed by the aforementioned software where the transient signal was recreated by simulating the vibrations and ionization signals simultaneously. The value that can be extracted from the data most directly is the change in central energy of each of the X-ray transition peaks as a result of vibrational dynamics. These shifts are on the order of 0.01 eV, which may seem quite small relative to the 0.1–0.2 eV resolution of the experiment. However, the resolution does not limit determining peak center energies, and the shifts in peak center induce quite large changes in ΔOD, as shown in Supplementary Fig. S1.

However, the peak center energy shifts alone do not define the desired CEPES slopes. It is also necessary to know the displacement along the vibrational coordinate or, in the case of the symmetric stretch, the C-Cl bond distance change induced by the pump pulse. That bond distance cannot be obtained directly from the XTAS data without prior knowledge of the CEPES, and so it needs to be estimated by other means. Typically, this stretch can be estimated from numerical solutions of the time-dependent Schrödinger equation if the time-dependent intensity profile of the pump pulse is very well known[81], but this estimation introduces far more uncertainty than the XTAS under the present setup. Precise knowledge of the pulse intensity is challenging on account of losses on the annular mirror used for pump-probe co-linearity, non-Gaussian focal spots due to the annular mirror, losses on the CCl_4 gas cell aperture, and perhaps most importantly, non-Gaussian temporal pulses. Because these experiments were undertaken with pump pulses close to a single cycle, third-order and higher dispersions have a large effect on the exact pulse envelope shape[82,83], and the tools to measure that envelope are not consistent enough in reconstruction to provide an exact pulse shape without error[84]. With these reservations, we numerically estimate the C-Cl bond length changes to be 0.0075 ± 0.0025 Å (i.e. ~33% error) at the $3 \pm 1 \times 10^{14}$ W/cm^2 pump intensity, utilizing Ehrenfest's theorem[85,86]. This is consistent with previously derived analytic results for Gaussian pump pulse envelopes[42].

It is possible to bypass errors in bond stretch estimation by comparing different core excited states relative to each other for a given data set, as the signal arises from the same vibrational motion. By normalizing to one of the

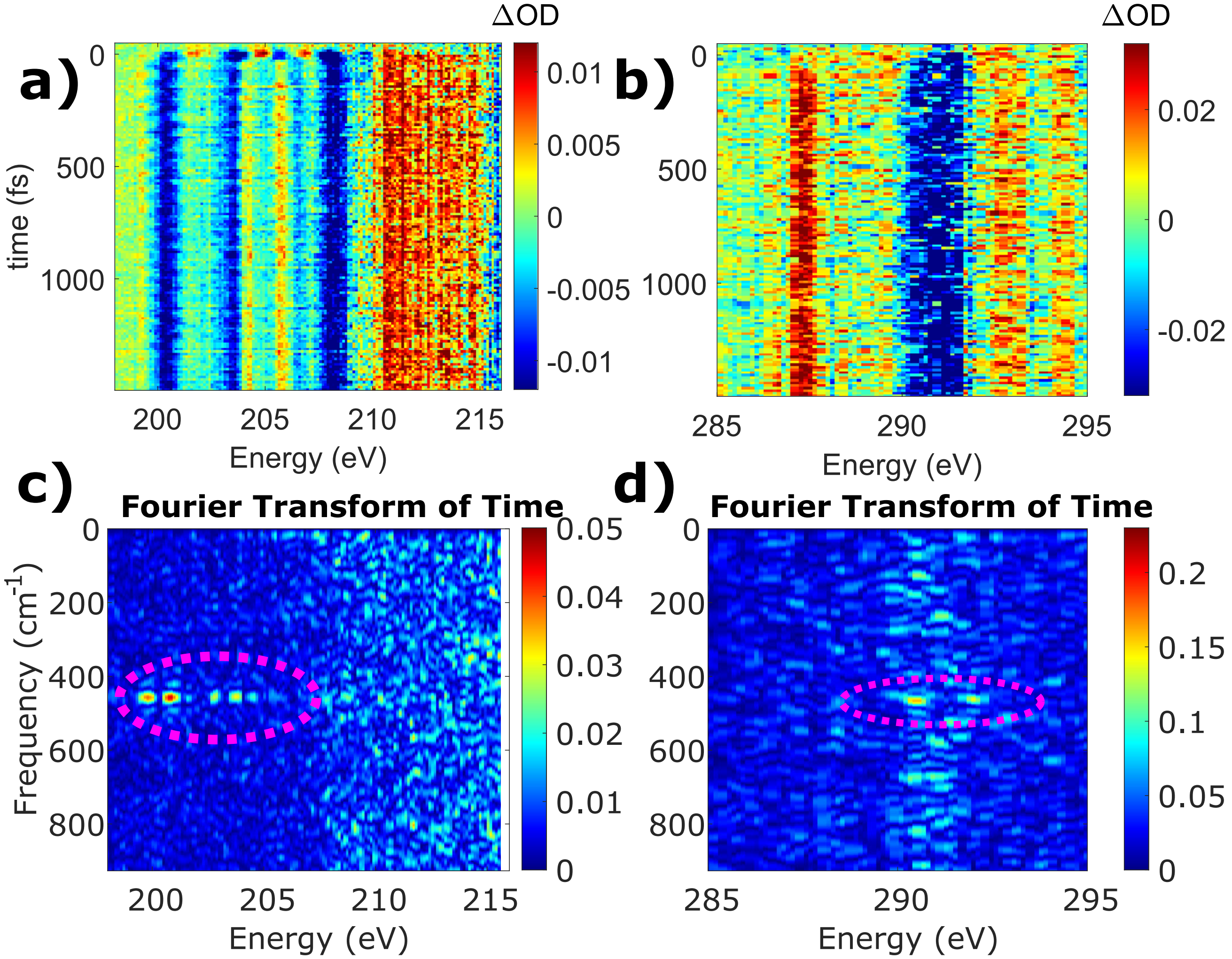

Fig. 3 | X-ray transient absorption following impulsive stimulated Raman scattering. a, b Example time domain ΔOD (change in optical density) data at the Cl $L_{2,3}$-edges and C K-edge, respectively. Positive time indicates pump arriving before probe. Positive (red) ΔOD signal indicates increased absorption, while negative (blue) indicates less absorption. The long-lived positive signals arise from dissociation products of CCl_4^+. Vibrational dynamics correspond to the oscillatory signals that are most clear around 200–205 eV. **c, d** The time domain data is Fourier transformed along the time axis at each energy. Only the v_1 mode frequency is visible at 450 cm^{-1} (with the pink dotted line aiding the eye). Other modes are not visible above the noise at or around 218 cm^{-1}, 791 cm^{-1}, nor 310 cm^{-1} (v_{2-4}, respectively), nor at the double of those frequencies. The positions of the vibrating electronic states are shown in Fig. 2 as peaks 1, 2, and C_1.

CEPES as discussed in the introduction (Eqn. (3)), the bond length stretch parameter can be eliminated. This allows comparison of the CEPES slopes purely based on the XTAS data. For the purposes of this paper, this means we define the slope of the first state, Cl $2p_{3/2} \rightarrow 7a_1^*$, to -1 eV/q, where q is an arbitrary bond stretch lengthscale. The negative sign is explicitly chosen as the core-level excitation energy to an antibonding orbital is expected to monotonically decrease with bond length increase[7,44,46,48,53], as the energy of the associated antibonding levels is lowered. The experimental relative slopes subsequently are: Cl $2p_{3/2} \rightarrow 7a_1^*$: -1, Cl $2p_{3/2} \rightarrow 8t_2^*$: -0.81 ± 0.08, and C $1s \rightarrow 8t_2^*$: -0.47 ± 0.05 (to 95% confidence), which are also shown in Table 3. The overlap of absorption features in the Cl $L_{2,3}$-edge static spectrum and the lower signal-to-noise, especially at the C K-edge, leads to somewhat sizeable error bars. These slopes show a significantly larger change for the Cl L-edge excitation energies along the normal mode coordinate, compared to the C K-edge excitation.

These experimental extracted relative slopes can be compared to absolute slopes from ROKS calculations. The computed absolute slopes for core-excitation energies vs C-Cl symmetric bond stretch are Cl $2p_{3/2} \rightarrow 7a_1^*$: -11.13 eV Å^{-1}, Cl $2p_{3/2} \rightarrow 8t_2^*$: -8.81 eV Å^{-1}, and C $1s \rightarrow 8t_2^*$: -5.30 eV Å^{-1}. The computed relative slopes for these states therefore are: Cl $2p_{3/2} \rightarrow 7a_1^*$: -1, Cl $2p_{3/2} \rightarrow 8t_2^*$: -0.79, and C $1s \rightarrow 8t_2^*$: -0.48, which agree very well with the experimental values (as shown in Table 3).

Encouraged by the strong agreement between experiment and theory for relative slopes, we apply the theoretical absolute values of CEPES slopes to the experimentally extracted relative values, which yields estimated experimental absolute slopes of Cl $2p_{3/2} \rightarrow 7a_1^*$: -11.13 eV Å^{-1}, Cl $2p_{3/2} \rightarrow 8t_2^*$: -9.0 eV Å^{-1}, and C $1s \rightarrow 8t_2^*$: -5.2 eV Å^{-1}. Both experi-

Table 3 | Slopes of core-excited potential energy surfaces along the symmetric stretch

Core-Excited Potential Energy Surfaces Slopes for v_1			
Slope	Experimental Relative	Calculation Relative	Calculation Absolute (in eV Å^{-1})
Cl $2p_{3/2} \rightarrow 7a_1^*$	-1	-1	-11.13
Cl $2p_{3/2} \rightarrow 8t_2^*$	-0.81 ± 0.08	-0.79	-8.81
C $1s \rightarrow 8t_2^*$	-0.47 ± 0.05	-0.48	-5.30

The experimentally extracted slopes for CCl_4, as compared to ROKS calculations.

mental relative slopes have ~ 10% uncertainty, and if we assume that this arises from equal percentage uncertainties for both the numerator and denominator, we obtain the 95% error bars to be ±0.8 eV Å^{-1}, ±0.6 eV Å^{-1}, and ±0.4 eV Å^{-1}, respectively, for the slopes of the three states. We note that the assumption that all three absolute slopes have the same relative uncertainty is not necessarily correct (especially considering the lower signal to noise in the C K-edge region), but the relative errors in the individual CEPES slopes are less than the ~ 10% error in the relative slopes, if the errors between slopes of different states are uncorrelated.

From the estimates for the absolute slopes, the amount of nuclear movement can also be estimated for each experimental data set. The smallest symmetric bond stretch amplitude across all data sets was 0.0018 Å and the largest was 0.0045 Å. These numbers seem very small, but they are close to the numeric solution of the Schrödinger equation, which yielded 0.0075 Å. The difference likely arises from errors in the expected intensity or deviations in the pump pulse shape from a perfect Gaussian envelope or, from an experimental perspective, the use of an incorrect pump pulse temporal broadening in the extraction. These bond length changes result in only ~ 0.05 eV changes in the absorption peak centers from the ground state, but the resulting transient signal is measurable by the experiment. The < 0.01 Å pump induced bond stretch also indicates that the first-order Taylor series approximation utilized in Eqn. (3) is likely valid, and higher order terms in bond stretch likely have a negligible impact on the transient X-ray absorption signal arising from vibrational dynamics of neutral CCl_4.

It is also interesting to consider why the CEPES slopes for the Cl $2p_{3/2} \rightarrow 7a_1^*$ and $2p_{3/2} \rightarrow 8t_2^*$ states are much larger than the corresponding slope for the C 1s→ $8t_2^*$ excitation. This can be possibly rationalized in terms of the composition of the antibonding orbital to which the core-electron is being excited, as the core-excitation energy is expected to be sensitive to this orbital. Subshell Löwdin population analysis[87] on the relaxed orbitals obtained from ROKS indicate that the $7a_1^*$ orbital of the Cl $2p_{3/2} \rightarrow 7a_1^*$ excited state and the $8t_2^*$ orbital of both the Cl $2p_{3/2} \rightarrow 8t_2^*$ and C 1s→ $8t_2^*$ excited states are of ~ 33−37% carbon character and ~ 63−67% Cl character. The greater contribution from Cl to these antibonding orbitals likely leads to the Cl 2p hole more strongly affecting the core-excitation potential than a C 1s hole, leading to larger slopes for Cl L-edge states than for the C K-edge states. We note that the Cl contribution to the antibonding levels is not very different for the Cl $2p_{3/2} \rightarrow 7a_1^*$ and $2p_{3/2} \rightarrow 8t_2^*$ excited states, and therefore this heuristic thus does not explain the 20% difference between the two Cl L-edge slopes. However, we believe that the large differences in behavior between CEPES slopes arising from different atom types in a molecule can be rationalized by an analysis of the composition of the orbital to which the core-electrons are being excited, post orbital relaxation in response to the formation of the core-hole.

The lack of signal from other vibrational modes

The Fourier transform of the experimental XTAS does not show any perceptible signal associated with the normal modes other than the symmetric stretch, despite all the modes being Raman active[71–73]. This behavior can arise either from the center of the vibrational wavepacket not coherently oscillating along asymmetric modes, or from very small CEPES slopes along these modes. We find both factors to be relevant for the present study.

CCl_4 has no permanent dipole and possesses an experimental[88] rotational constant of 0.057 cm^{-1}. The molecule consequently cannot rotationally reorient within the duration of the 6 fs FWHM 800 nm pump pulse and thus experiences a spatially isotropic electric field $\mathcal{E}(t)$ that lowers the energy by $\frac{1}{2}\alpha_{iso}(\{q_i\})|\mathcal{E}(t)|^2$ (where $\alpha_{iso}(\{q_i\})$ is the isotropic polarizability). Small bond stretches are induced by $\mathcal{E}(t)$ as the resulting increase in polarizability[89] can provide stabilization. It is however not possible for an isotropic electric field to spontaneously break the T_d symmetry of CCl_4, implying that $\left(\frac{d\alpha_{iso}}{dq_i}\right)_{\{q_i\}=0} = 0$ for the asymmetric modes. Ehrenfest's theorem[85,86] therefore indicates that there is no field-induced force to displace the center of the vibrational wavefunction along the asymmetric modes, and ISRS cannot produce coherent oscillation of the wavefunction center[42] (see Supplementary Notes 2 and 3). This is confirmed by time-dependent Schrödinger equation simulations utilizing the full polarizability tensor (shown in Supplementary Note 4), which demonstrate that the wavepacket center position $\langle\{q_i\}\rangle(t)$ only oscillates along the symmetric stretch. ISRS can however produce oscillations in the spatial width of the wavefunction along all normal modes, which occur at twice the normal mode frequency.

In addition, we note that small displacements in the wavepacket center along the asymmetric modes would nonetheless not lead to a strong response in the XTAS for CCl_4 because of degeneracies between core-excited states that contribute to the spectral features. The C 1s→ $8t_2^*$ excitation is triply degenerate and the individual constituent states should therefore possess CEPES forces along some asymmetric modes from the Jahn-Teller effect[90]. However, the observed C_1 peak in Fig. 2 would not separate into three distinct, non-overlapping entities in the limit of small asymmetric mode displacements and any observed shift in the peak center position would represent an average over all three core-excited states. This scenario also applies to the Cl L-edge, where the presence of 4 Cl atoms similarly leads to a number of degenerate or nearly degenerate states that contribute to the observed spectral features like Peaks 1 and 2 in Fig. 2. It is possible for the individual states to have CEPES slopes of opposite signs along asymmetric modes (e.g. an asymmetric stretching mode elevating the energy of one C 1s→ $8t_2^*$ state while reducing the energy of the other two), leading to small *average* slopes and consequently small shifts in the peak center energy.

To investigate effects of averaging CEPES slopes over (nearly) degenerate core-excited states, we have performed nonrelativistic CEPES gradient calculations with ROKS[19,91] for all three C 1s→ $8t_2^*$ excitations and for all twelve possible Cl 2p→ $7a_1^*$ excitations. Projecting these gradients onto unit vectors along each normal mode direction shows that CEPES slopes averaged over all C 1s→ $8t_2^*$ or Cl 2p→ $7a_1^*$ excitations are essentially zero (~ 0.03 eV Å^{-1} or smaller, as shown in Supplementary Note 5) along the asymmetric modes. We do note that even though the average slope along any asymmetric mode is quite small, individual C 1s and Cl 2p excited states may have substantial slopes along some modes. This could lead to time-dependent changes in the width of XTAS features as the energies of the constituent states move further apart (closer together) with displacement from (towards) T_d symmetry. Such effects should lead to signal at twice the normal mode frequency, but were not experimentally detected above the noise.

These issues raise an important question as to whether all vibrational modes can be reliably measured with XTAS in general molecular systems. In our view, a system with reduced symmetry where core-excitation energies are well-separated ought not to show either of the previously discussed issues. For instance, all the vibrational modes of a molecule like CFClBrI will be totally symmetric (*a* symmetry) and the C 1s absorption features will arise from nondegenerate core-level excitations. Such a molecule would therefore be ideal for CEPES slope measurements with XTAS subsequent to vibrational activation. Conversely, symmetric stretching oscillations may cause the strongest signal by orders of magnitude in highly symmetric molecules, as was previously observed in ISRS-XTAS measurements on the SF_6 molecule[53]. It would nonetheless be quite helpful to have a significant force/slope on the CEPES at the equilibrium geometry, suggesting that core-level excitations involving antibonding orbitals would be ideal targets.

Conclusions

In this work, the impulsive stimulated Raman scattering induced coherent vibrations of CCl_4 have been studied with X-ray transient absorption spectroscopy, and linear slopes of the core-excited potential energy surfaces along the totally symmetric bond stretching mode have been extracted. Normalizing to the first state, these are Cl $2p_{3/2} \rightarrow 7a_1^*$: −1, Cl $2p_{3/2} \rightarrow 8t_2^*$: −0.81 ± 0.08, and C 1s→ $8t_2^*$: −0.47 ± 0.05, which compares well with theoretical values of −1, −0.79, and −0.48, respectively. Scaling the experimental relative slopes to the theoretical absolute slopes give

-11.1 ± 0.8 eV $\AA^{-1}$, -9.0 ± 0.6 eV $\AA^{-1}$, and -5.2 ± 0.4 eV $\AA^{-1}$, respectively. These slopes indicate a small ISRS induced totally symmetric bond elongation of < 0.01 Å, in conjunction with the experimentally observed shifts in peak center energies (~0.05 eV). Displacements on this scale[53] or even smaller scales[54] were previously reported for SF_6. The ability of XTAS to report on the dynamics arising from such small displacements indicates the sensitivity of this approach for studying the X-ray potential response to the dynamics of nuclear motion, potentially permitting detection of femtometer scale changes.

The larger slopes for Cl L-edge excitations relative to the C K-edge excitation is likely a result of the excited electron occupancy of the $7a_1^*/8t_2^*$ levels that ROKS calculations indicate have a ~33% contribution from C and ~66% contribution from Cl and thereby are more sensitive to the presence of a Cl core hole. It would be interesting to explore whether similar relationships between CEPES slopes can be observed in other molecules where multiple different inner-shell edges can be probed.

We note that no XTAS signal from vibrational dynamics from other normal modes of CCl_4 is experimentally detected. This appears to be a consequence of the ISRS process not displacing the center of the vibrational wavefunction along these modes. It also appears that there is no or little CEPES slope along the asymmetric modes after averaging over all (near) degenerate core-level excited states that contribute to the observed spectral features, leading to lack of transient X-ray signal under current experimental conditions, which would also present issues in molecules of other symmetries with many degenerate orbitals. Less symmetric molecules with well-resolved core-excitation energies at the equilibrium geometry would be unlikely to have such issues and therefore are likely to reveal XTAS signals corresponding to vibrational dynamics of many more modes. Strong XTAS signal is particularly likely for species with low lying valence antibonding orbitals like other halogenated molecules or conjugated organic species, as excitations from core-levels to such orbitals are likely to lead to large CEPES slopes at the equilibrium geometry.

Data availability

The Supplementary Information contains additional information about the experiment and the time-dependent Schrödinger equation simulations, as well as the results from these simulations (PDF). The computed X-ray absorption energies at various (symmetric) bond distances that were used to obtain the computed slopes are also provided (Supplementary Data 1, XLXS). The ground state equilibrium geometry, the molecular orbitals optimized by ROKS at this geometry, and the results of the the time-dependent Schrödinger equation simulations have been made publicly available via Zenodo[92].

Code availability

The code for the time-dependent Schrödinger equation simulations have been made publicly available via Zenodo[92].

Received: 8 May 2024; Accepted: 30 August 2024;

References

1. Bhattacherjee, A. & Leone, S. R. Ultrafast x-ray transient absorption spectroscopy of gas-phase photochemical reactions: A new universal probe of photoinduced molecular dynamics. *Acc. Chem. Res.* **51**, 3203–3211 (2018).
2. Geneaux, R., Marroux, H. J. B., Guggenmos, A., Neumark, D. M. & Leone, S. R. Transient absorption spectroscopy using high harmonic generation: a review of ultrafast x-ray dynamics in molecules and solids. *Philos. Trans. R. Soc. A: Math., Phys. Eng. Sci.* **377**, 20170463 (2019).
3. Bressler, C. & Chergui, M. Ultrafast x-ray absorption spectroscopy. *Chem. Rev.* **104**, 1781–1812 (2004).
4. De Groot, F. High-resolution x-ray emission and x-ray absorption spectroscopy. *Chem. Rev.* **101**, 1779–1808 (2001).
5. Wollan, E. O. X-ray scattering and atomic structure. *Rev. Mod. Phys.* **4**, 205 (1932).
6. Attar, A. R. et al. Femtosecond x-ray spectroscopy of an electrocyclic ring-opening reaction. *Science* **356**, 54–59 (2017).
7. Ross, A. D. et al. Jahn-Teller distortion and dissociation of CCl_4 by transient x-ray spectroscopy simultaneously at the carbon K-and chlorine L-edge. *Chem. Sci.* **13**, 9310–9320 (2022).
8. Henderson, G. S., De Groot, F. M. & Moulton, B. J. X-ray absorption near-edge structure (xanes) spectroscopy. *Rev. Mineral. Geochem.* **78**, 75–138 (2014).
9. Schülke, W. *Electron dynamics by inelastic X-ray scattering*, vol. 7 (OUP Oxford, 2007).
10. Hähner, G. Near edge x-ray absorption fine structure spectroscopy as a tool to probe electronic and structural properties of thin organic films and liquids. *Chem. Soc. Rev.* **35**, 1244–1255 (2006).
11. Gaffney, K. & Chapman, H. N. Imaging atomic structure and dynamics with ultrafast x-ray scattering. *Science* **316**, 1444–1448 (2007).
12. Kraus, P. M., Zürch, M., Cushing, S. K., Neumark, D. M. & Leone, S. R. The ultrafast x-ray spectroscopic revolution in chemical dynamics. *Nat. Rev. Chem.* **2**, 82–94 (2018).
13. Bressler, C. & Chergui, M. Molecular structural dynamics probed by ultrafast x-ray absorption spectroscopy. *Annu. Rev. Phys. Chem.* **61**, 263–282 (2010).
14. Ridente, E. et al. Femtosecond symmetry breaking and coherent relaxation of methane cations via x-ray spectroscopy. *Science* **380**, 713–717 (2023).
15. Zinchenko, K. S. et al. Sub-7-femtosecond conical-intersection dynamics probed at the carbon K-edge. *Science* **371**, 489–494 (2021).
16. Pertot, Y. et al. Time-resolved x-ray absorption spectroscopy with a water window high-harmonic source. *Science* **355**, 264–267 (2017).
17. Haugen, E. A. et al. Ultrafast x-ray spectroscopy of intersystem crossing in hexafluoroacetylacetone: Chromophore photophysics and spectral changes in the face of electron-withdrawing groups. *J. Phys. Chem. A* **127**, 634–644 (2023).
18. Li, S. et al. Attosecond-pump attosecond-probe x-ray spectroscopy of liquid water. *Science* **383**, 1118–1122 (2024).
19. Hait, D. & Head-Gordon, M. Highly accurate prediction of core spectra of molecules at density functional theory cost: Attaining sub-electronvolt error from a restricted open-shell Kohn–Sham approach. *J. Phys. Chem. Lett.* **11**, 775–786 (2020).
20. Hait, D. et al. Accurate prediction of core-level spectra of radicals at density functional theory cost via square gradient minimization and recoupling of mixed configurations. *J. Chem. Phys.* **153**, 134108 (2020).
21. Wenzel, J., Wormit, M. & Dreuw, A. Calculating core-level excitations and x-ray absorption spectra of medium-sized closed-shell molecules with the algebraic-diagrammatic construction scheme for the polarization propagator. *J. Comput. Chem.* **35**, 1900–1915 (2014).
22. Oosterbaan, K. J., White, A. F. & Head-Gordon, M. Non-orthogonal configuration interaction with single substitutions for the calculation of core-excited states. *J. Chem. Phys.* **149**, 044116 (2018).
23. Vidal, M. L., Feng, X., Epifanovsky, E., Krylov, A. I. & Coriani, S. New and efficient equation-of-motion coupled-cluster framework for core-excited and core-ionized states. *J. Chem. Theory Comput.* **15**, 3117–3133 (2019).
24. Besley, N. A. Modeling of the spectroscopy of core electrons with density functional theory. *Wiley Interdiscip. Rev. Comput. Mol. Sci.* **11**, e1527 (2021).
25. Norman, P. & Dreuw, A. Simulating x-ray spectroscopies and calculating core-excited states of molecules. *Chem. Rev.* **118**, 7208–7248 (2018).
26. Garner, S. M., Haugen, E. A., Leone, S. R. & Neuscamman, E. Spin coupling effect on geometry-dependent x-ray absorption of diradicals. *J. Am. Chem. Soc.* **146**, 2387–2397 (2024).

27. Yao, Y., Golze, D., Rinke, P., Blum, V. & Kanai, Y. All-electron BSE@GW method for K-edge core electron excitation energies. *J. Chem. Theory Comput.* **18**, 1569–1583 (2022).
28. Carter-Fenk, K., Cunha, L. A., Arias-Martinez, J. E. & Head-Gordon, M. Electron-affinity time-dependent density functional theory: Formalism and applications to core-excited states. *J. Phys. Chem. Lett.* **13**, 9664–9672 (2022).
29. Pinjari, R. V., Delcey, M. G., Guo, M., Odelius, M. & Lundberg, M. Restricted active space calculations of L-edge x-ray absorption spectra: From molecular orbitals to multiplet states. *J. Chem. Phys*. **141**, 124116 (2014).
30. Guo, M., Sørensen, L. K., Delcey, M. G., Pinjari, R. V. & Lundberg, M. Simulations of iron K pre-edge x-ray absorption spectra using the restricted active space method. *Phys. Chem. Chem. Phys.* **18**, 3250–3259 (2016).
31. Kasper, J. M., Stetina, T. F., Jenkins, A. J. & Li, X. Ab initio methods for l-edge x-ray absorption spectroscopy. *Chem. Phys. Rev*. **1**, 011304 (2020).
32. Montorsi, F., Segatta, F., Nenov, A., Mukamel, S. & Garavelli, M. Soft x-ray spectroscopy simulations with multiconfigurational wave function theory: Spectrum completeness, sub-ev accuracy, and quantitative reproduction of line shapes. *J. Chem. Theory Comput.* **18**, 1003–1016 (2022).
33. Vacher, M., Kunnus, K., Delcey, M. G., Gaffney, K. J. & Lundberg, M. Origin of core-to-core x-ray emission spectroscopy sensitivity to structural dynamics. *Struct. Dyn*.**7** (2020).
34. Prince, K. C., Richter, R., de Simone, M., Alagia, M. & Coreno, M. Near edge x-ray absorption spectra of some small polyatomic molecules. *J. Phys. Chem. A* **107**, 1955–1963 (2003).
35. Vaz da Cruz, V. et al. Nuclear dynamics in resonant inelastic x-ray scattering and x-ray absorption of methanol. *J. Chem. Phys.* **150**, 234301 (2019).
36. Hait, D. & Martínez, T. J. Predicting the x-ray absorption spectrum of ozone with single configuration state functions. *J. Chem. Theory Comput.* **20**, 873–881 (2024).
37. Itoh, S.-i, Tanaka, S. & Kayanuma, Y. Vibronic theory for the x-ray absorption spectrum of CF_4 molecules. *Phys. Rev. A* **60**, 4488 (1999).
38. Olovsson, W. et al. Vibrational effects in x-ray absorption spectra of two-dimensional layered materials. *J. Phys. Chem. C.* **123**, 9688–9692 (2019).
39. Morzan, U. N., Videla, P. E., Soley, M. B., Nibbering, E. T. & Batista, V. S. Vibronic dynamics of photodissociating icn from simulations of ultrafast x-ray absorption spectroscopy. *Angew. Chem.* **132**, 20219–20223 (2020).
40. Takahashi, O., Yamamura, R., Tokushima, T. & Harada, Y. Interpretation of the x-ray emission spectra of liquid water through temperature and isotope dependence. *Phys. Rev. Lett.* **128**, 086002 (2022).
41. Cruzeiro, V. W. D., Hait, D., Shea, J., Hohenstein, E. G. & Martinez, T. J. $1b_1$ splitting in the x-ray emission spectrum of liquid water is dominated by ultrafast dissociation. *ChemRxiv* https://doi.org/10.26434/chemrxiv-2023-5jvl5 (2023).
42. Yan, Y.-X., Gamble Jr, E. B. & Nelson, K. A. Impulsive stimulated scattering: General importance in femtosecond laser pulse interactions with matter, and spectroscopic applications. *J. Chem. Phys.* **83**, 5391–5399 (1985).
43. Yan, Y.-X. & Nelson, K. A. Impulsive stimulated light scattering. I. General theory. *J. Chem. Phys.* **87**, 6240–6256 (1987).
44. Miron, C. et al. Imaging molecular potentials using ultrahigh-resolution resonant photoemission. *Nat. Phys.* **8**, 135–138 (2012).
45. Kimberg, V. & Miron, C. Molecular potentials and wave function mapping by high-resolution electron spectroscopy and ab initio calculations. *J. Electron Spectrosc. Relat. Phenom.* **195**, 301–306 (2014).
46. Schreck, S. et al. Ground state potential energy surfaces around selected atoms from resonant inelastic x-ray scattering. *Sci. Rep.* **6**, 1–8 (2016).
47. Eckert, S. et al. One-dimensional cuts through multidimensional potential-energy surfaces by tunable x rays. *Phys. Rev. A* **97**, 053410 (2018).
48. Vaz da Cruz, V. et al. Probing hydrogen bond strength in liquid water by resonant inelastic x-ray scattering. *Nat. Commun.* **10**, 1–9 (2019).
49. Saito, N. et al. Real-time observation of electronic, vibrational, and rotational dynamics in nitric oxide with attosecond soft x-ray pulses at 400 eV. *Optica* **6**, 1542–1546 (2019).
50. Weisshaupt, J. et al. Ultrafast modulation of electronic structure by coherent phonon excitations. *Phys. Rev. B* **95**, 081101 (2017).
51. Cammarata, M. et al. Sequential activation of molecular breathing and bending during spin-crossover photoswitching revealed by femtosecond optical and x-ray absorption spectroscopy. *Phys. Rev. Lett.* **113**, 227402 (2014).
52. Mincigrucci, R. et al. Element-and enantiomer-selective visualization of molecular motion in real-time. *Nat. Commun.* **14**, 386 (2023).
53. Barreau, L. et al. Core-excited states of SF_6 probed with soft-x-ray femtosecond transient absorption of vibrational wave packets. *Phys. Rev. A* **108**, 012805 (2023).
54. Rupprecht, P. et al. Resolving vibrations in a polyatomic molecule with femtometer precision via x-ray spectroscopy. *Phys. Rev. A* **108**, 032816 (2023).
55. Lu, K. et al. Core-level anionic photofragmentation of gaseous CCl_4 and solid-state analogs. *Phys. Rev. A* **80**, 033406 (2009).
56. Fock, J.-H. & Koch, E.-E. Shape resonances and partial photoemission cross sections of solid SF_6 and CCl_4. *Chem. Phys.* **96**, 125–143 (1985).
57. Frank, I., Hutter, J., Marx, D. & Parrinello, M. Molecular dynamics in low-spin excited states. *J. Chem. Phys.* **108**, 4060–4069 (1998).
58. Barreau, L. et al. Efficient table-top dual-wavelength beamline for ultrafast transient absorption spectroscopy in the soft x-ray region. *Sci. Rep.* **10**, 5773 (2020).
59. Fidler, A. P. et al. Nonlinear xuv signal generation probed by transient grating spectroscopy with attosecond pulses. *Nat. Commun.* **10**, 1384 (2019).
60. Géneaux, R., Chang, H.-T., Schwartzberg, A. M. & Marroux, H. J. B. Source noise suppression in attosecond transient absorption spectroscopy by edge-pixel referencing. *Opt. Express* **29**, 951–960 (2021).
61. Ott, C. et al. Reconstruction and control of a time-dependent two-electron wave packet. *Nature* **516**, 374 (2014).
62. Epifanovsky, E. et al. Software for the frontiers of quantum chemistry: An overview of developments in the Q-Chem 5 package. *J. Chem. Phys.* **155**, 084801 (2021).
63. Hui, K. & Chai, J.-D. SCAN-based hybrid and double-hybrid density functionals from models without fitted parameters. *J. Chem. Phys.* **144**, 044114 (2016).
64. Hait, D. & Head-Gordon, M. Orbital optimized density functional theory for electronic excited states. *J. Phys. Chem. Lett.* **12**, 4517–4529 (2021).
65. Hait, D. & Head-Gordon, M. How accurate are static polarizability predictions from density functional theory? An assessment over 132 species at equilibrium geometry. *Phys. Chem. Chem. Phys.* **20**, 19800–19810 (2018).
66. Jensen, F. Unifying general and segmented contracted basis sets. Segmented polarization consistent basis sets. *J. Chem. Theory Comput.* **10**, 1074–1085 (2014).
67. Ambroise, M. A. & Jensen, F. Probing basis set requirements for calculating core ionization and core excitation spectroscopy by the Δ self-consistent-field approach. *J. Chem. Theory Comput.* **15**, 325–337 (2018).

68. Cunha, L. A., Hait, D., Kang, R., Mao, Y. & Head-Gordon, M. Relativistic orbital-optimized density functional theory for accurate core-level spectroscopy. *J. Phys. Chem. Lett.* **13**, 3438–3449 (2022).
69. Saue, T. Relativistic hamiltonians for chemistry: A primer. *ChemPhysChem* **12**, 3077–3094 (2011).
70. Hait, D. & Head-Gordon, M. Excited state orbital optimization via minimizing the square of the gradient: General approach and application to singly and doubly excited states via density functional theory. *J. Chem. Theory Comput.* **16**, 1699–1710 (2020).
71. Welsh, H., Crawford, M., Thomas, T. & Love, G. Raman spectroscopy of low pressure gases and vapors. *Can. J. Phys.* **30**, 577–596 (1952).
72. Chakraborty, T. & Verma, A. Vibrational spectra of CCl_4: isotopic components and hot bands. part I. *Spectrochimica Acta Part A: Mol. Biomolecular Spectrosc.* **58**, 1013–1023 (2002).
73. Chakraborty, T. & Rai, S. N. Comparative study of infrared and Raman spectra of CCl_4 in vapour and condensed phases: Effect of LO-TO splitting resulting from hetero-isotopic TD-TD interactions. *Spectrochimica Acta Part A: Mol. Biomolecular Spectrosc.* **65**, 406–413 (2006).
74. Teodorescu, C., Esteva, J., Karnatak, R. & El Afif, A. An approximation of the Voigt I profile for the fitting of experimental x-ray absorption data. *Nucl. Instrum. Methods Phys. Res. Sect. A: Accelerators, Spectrometers, Detect. Associated Equip.* **345**, 141–147 (1994).
75. Iwamitsu, K. et al. Spectral analysis of x-ray absorption near edge structure in α-Fe_2O_3 based on bayesian spectroscopy. *Phys. status solidi (b)* **257**, 2000107 (2020).
76. Briggs, D. & Grant, J. T. *Surface analysis by Auger and X-ray photoelectron spectroscopy* (SurfaceSpectra, 2012).
77. Hudson, E. et al. High-resolution measurements of near-edge resonances in the core-level photoionization spectra of SF_6. *Phys. Rev. A* **47**, 361–373 (1993).
78. Hitchcock, A. & Brion, C. Inner-shell excitation and exafs-type phenomena in the chloromethanes. *J. Electron Spectrosc. Relat. Phenom.* **14**, 417–441 (1978).
79. Lu, K. et al. State-specific dissociation enhancement of ionic and excited neutral photofragments of gaseous CCl_4 and solid-state analogs following Cl 2p core-level excitation. *N. J. Phys.* **10**, 053009 (2008).
80. Gaynor, J. D., Wetterer, A. M., Cochran, R. M., Valente, E. J. & Mayer, S. G. Vibrational spectroscopy of the CCl_4 v_1 mode: Theoretical prediction of isotopic effects. *J. Chem. Educ.* **92**, 1081–1085 (2015).
81. Schmidt, B. & Hartmann, C. Wavepacket: A matlab package for numerical quantum dynamics. II: Open quantum systems, optimal control, and model reduction. *Computer Phys. Commun.* **228**, 229–244 (2018).
82. Hong, K.-H. & Nam, C. H. Adaptive pulse compression of femtosecond laser pulses using a low-loss pulse shaper. *Jpn. J. Appl. Phys.* **43**, 5289 (2004).
83. Meng, Y., Zhang, S., Jin, C., Li, H. & Wang, X. Enhanced compression of femtosecond pulse in hollow-core photonic bandgap fibers. *Opt. Commun.* **283**, 2411–2415 (2010).
84. Miranda, M. et al. Characterization of broadband few-cycle laser pulses with the d-scan technique. *Opt. express* **20**, 18732–18743 (2012).
85. Ehrenfest, P. Bemerkung über die angenäherte gültigkeit der klassischen mechanik innerhalb der quantenmechanik. *Z. f. ür. Phys.* **45**, 455–457 (1927).
86. Shankar, R. *Principles of quantum mechanics* (Springer Science & Business Media, 2012).
87. Löwdin, P.-O. On the non-orthogonality problem connected with the use of atomic wave functions in the theory of molecules and crystals. *J. Chem. Phys.* **18**, 365–375 (1950).
88. Yamamoto, S., Takami, M. & Kuchitsu, K. Diode laser spectroscopy of the v_3 band of carbon tetrachloride ($C^{35}Cl_4$): Stark modulation and cold jet infrared absorption spectrum. *J. Chem. Phys.* **81**, 3800–3804 (1984).
89. Hait, D. & Head-Gordon, M. When is a bond broken? The polarizability perspective. *Angew. Chem. Int. Ed.* **62**, e202312078 (2023).
90. Jahn, H. A. & Teller, E. Stability of polyatomic molecules in degenerate electronic states I-Orbital degeneracy. *Proc. R. Soc. Lond. Ser. A-Math. Phys. Sci.* **161**, 220–235 (1937).
91. Kowalczyk, T., Tsuchimochi, T., Chen, P.-T., Top, L. & Van Voorhis, T. Excitation energies and stokes shifts from a restricted open-shell Kohn-Sham approach. *J. Chem. Phys.* **138**, 164101 (2013).
92. Ross, A. et al. Computational data for 'Measurement of Coherent Vibrational Dynamics with X-ray Transient Absorption Spectroscopy Simultaneously at the Carbon K- and Chlorine $L_{2,3}$- Edges' https://doi.org/10.5281/zenodo.11153002 (2024).

Acknowledgements

This work is funded by the DOE Office of Science, Basic Energy Science (BES) Program, Chemical Sciences, Geosciences and Biosciences Division under Contract no. DE-AC02-05CH11231, through the Gas Phase Chemical Physics program (ADR, VS, DMN, SRL) and Atomic, Molecular, and Optical Sciences program (DH and MHG). The instrument was built with funds from the National Science Foundation through NSF MRI 1624322 and matching funds from the Lawrence Berkeley National Laboratory, the College of Chemistry, the Department of Physics, and the Vice Chancellor for Research at UC Berkeley. This research used resources of the National Energy Research Scientific Computing Center, a DOE Office of Science User Facility supported by the Office of Science of the U.S. Department of Energy under Contract No. DE-AC02-05CH11231 using NERSC award BES-ERCAP0027716. ADR was additionally funded by the U.S. Department of Energy, Office of Science, Office of Basic Energy Sciences, Materials Sciences and Engineering Division, under Contract No. DE-AC02-05-CH11231 within the Physical Chemistry of Inorganic Nanostructures Program (KC3103), by the W. M. Keck Foundation Grant No. 042982, and by the U.S. Army Research Office (ARO) under Grant No. W911NF-20-1-0127. SRL acknowledges related support of NSF grant CHE-2243756.

Author contributions

Experimental investigation: A.D.R. and V.S. Theoretical investigation: D.H. Code development: D.H. and A.D.R. Experiment supervision: S.R.L. and D.M.N. Theory supervision: M.H.G. Writing - original draft: A.D.R. and D.H. Writing - review & editing: A.D.R., D.H., V.S., D.M.N., M.H.G., and S.R.L.

Competing interests

The authors declare the following competing interest: M.H.G. is a part-owner of Q.-Chem, which is the software platform in which the quantum chemical calculations were carried out. All other authors declare no competing interests.

Additional information

Supplementary information The online version contains supplementary material available at https://doi.org/10.1038/s42005-024-01794-4.

Correspondence and requests for materials should be addressed to Stephen R. Leone.

Peer review information *Communications Physics* thanks Oriol Vendrell and the other, anonymous, reviewer(s) for their contribution to the peer review of this work.